CMS Physics Analysis Summary

Search for new physics in the all-hadronic final state with the MT2 variable

The CMS Collaboration

Abstract

A search for new physics is performed using events with jets and a large transverse momentum imbalance, as measured through the M_{T2} variable. The results are based on a sample of proton-proton collisions collected in 2016 at a center-of-mass energy of 13 TeV with the CMS detector and corresponding to an integrated luminosity of 35.9 fb^{-1}. No excess above the standard model background is observed. The results are interpreted as limits on the masses of potential new particles in a variety of simplified models of R-parity conserving supersymmetry. Depending on the details of the model, 95% CL lower limits on the gluino and light-flavor squark masses are placed up to 2025 and 1550 GeV, respectively. In the case of top (bottom) squarks, the mass limits are as high as 1070 (1175) GeV.

1 Introduction

We present the result of a search for new physics in events with jets and significant transverse momentum imbalance. Such searches were previously conducted by both the ATLAS [1–4] and CMS [5–8] collaborations using datasets of 13 TeV proton-proton (pp) collisions. This search builds on the work presented in Ref. [5], using improved methods and a dataset corresponding to an integrated luminosity of 35.9 fb^{-1} of pp collisions collected during 2016 at a center-of-mass energy of 13 TeV with the CMS detector at the CERN LHC. Event counts in bins of the number of jets (N_j), the number of b-tagged jets (N_b), the scalar sum of the transverse momenta p_T of all selected jets (H_T), and the M_T2 variable [5, 9] are compared against data-driven estimates of the background from standard model (SM) processes. We observe no evidence for an excess above the expected background and interpret the result as limits on the production of pairs of gluinos and squarks using simplified models of supersymmetry (SUSY). Model-independent limits on the number of non-SM events are also provided for a set of simplified, inclusive search regions.

2 The CMS detector

A more detailed description of the CMS detector, together with a definition of the coordinate system used and the relevant kinematic variables, can be found in Ref. [10]. The central feature of the CMS apparatus is a superconducting solenoid of 6 m internal diameter, providing a magnetic field of 3.8 T. Within the solenoid volume are a silicon pixel and strip tracker, a lead tungstate crystal electromagnetic calorimeter, and a brass and scintillator hadron calorimeter, each composed of a barrel and two endcap sections. Forward calorimeters extend the pseudorapidity (η) coverage provided by the barrel and endcap detectors. Muons are measured in gas-ionization detectors embedded in the steel flux-return yoke outside the solenoid. The first level of the CMS trigger system, composed of custom hardware processors, uses information from the calorimeters and muon detectors to select the most interesting events in a fixed time interval of less than 4 μs. The high-level trigger processor farm further decreases the event rate from around 100 kHz to less than 1 kHz, before data storage.

3 Event selection and Monte Carlo simulation

The physics objects and the event preselection are similar to those in Ref. [5] and are summarized in Table 1. We select events with at least one jet and veto events with an isolated lepton or charged particle-flow candidate. Jets are formed by clustering particle-flow candidates using the anti-k_T algorithm [11] and are corrected for contributions from pileup [12] and to account for non-uniform detector response. Jets consistent with originating from a heavy-flavor hadron are identified using the CSVv2 tagging algorithm [13], with a working point chosen such that the efficiency to identify a b quark jet is in the range 50–65% for jet transverse momentum (p_T) between 20 and 400 GeV. The misidentification rate for light-quark and gluon jets is approximately 1%.

The negative of the vector sum of the p_T of all selected jets is denoted by $\vec{H}_\mathrm{T}^{\mathrm{miss}}$, while $\vec{p}_\mathrm{T}^{\mathrm{miss}}$ is defined as the negative of the vector sum of all reconstructed particle-flow candidates. The jet corrections are propagated as a correction to $\vec{p}_\mathrm{T}^{\mathrm{miss}}$, and events with possible contributions from beam halo processes or anomalous noise in the calorimeter are rejected using dedicated filters [14]. For events with at least two jets, we cluster the jets into two pseudo-jets following Ref. [5] and calculate the kinematic variable M_T2 as

$$M_{T2} = \min_{\vec{p}_T^{\text{miss}X(1)} + \vec{p}_T^{\text{miss}X(2)} = \vec{p}_T^{\text{miss}}} \left[\max \left(M_T^{(1)}, M_T^{(2)} \right) \right], \tag{1}$$

where $\vec{p}_T^{\text{miss}X(i)}$ (with i=1,2) are trial vectors obtained by decomposing $\vec{p}_T^{\text{miss}}$ and $M_T^{(i)}$ are the transverse masses obtained by pairing any of these trial vectors with one of the two pseudojets. The minimization is performed over all trial momenta satisfying the $\vec{p}_T^{\text{miss}}$ constraint.

Table 1: Summary of objects and preselection. R is the distance parameter of the anti-k_t algorithm[15, 16] used to cluster particle flow [17, 18] candidates into jets. For veto leptons and tracks, the transverse mass M_T is determined using the veto object and the $\vec{p}_T^{\text{miss}}$, while p_T^{sum} denotes the sum of the transverse momenta of all the particle candidates around the lepton or track. Details of the lepton selection are described in Ref. [5]. The ith highest p_T jet is denoted as j_i.

Trigger	$p_T^{\text{miss}} > 120\,\text{GeV}$ and $H_T^{\text{miss}} > 120\,\text{GeV}$ or
	$H_T > 300\,\text{GeV}$ and $p_T^{\text{miss}} > 110\,\text{GeV}$ or
	$H_T > 900\,\text{GeV}$ or jet $p_T > 450\,\text{GeV}$
Jet selection	$R < 0.4$, $p_T > 30\,\text{GeV}$, $|\eta| < 2.4$
b-tag selection	$p_T > 20\,\text{GeV}$, $|\eta| < 2.4$
p_T^{miss}	$p_T^{\text{miss}} > 250\,\text{GeV}$ for $H_T < 1000\,\text{GeV}$, else $p_T^{\text{miss}} > 30\,\text{GeV}$
	$\Delta\phi \left(p_T^{\text{miss}}, j_{1,2,3,4} \right) > 0.3$
	$|\vec{p}_T^{\text{miss}} - \vec{H}_T^{\text{miss}}| / p_T^{\text{miss}} < 0.5$
M_{T2}	$M_{T2} > 200\,\text{GeV}$ for $H_T < 1500\,\text{GeV}$, else $M_{T2} > 400\,\text{GeV}$
Veto muon	$p_T > 10\,\text{GeV}$, $|\eta| < 2.4$, $p_T^{\text{sum}} < 0.2 \times p_T^{\text{lep}}$ or
	$p_T > 5\,\text{GeV}$, $|\eta| < 2.4$, $M_T < 100\,\text{GeV}$, $p_T^{\text{sum}} < 0.2 \times p_T^{\text{lep}}$
Veto electron	$p_T > 10\,\text{GeV}$, $|\eta| < 2.4$, $p_T^{\text{sum}} < 0.1 \times p_T^{\text{lep}}$ or
	$p_T > 5\,\text{GeV}$, $|\eta| < 2.4$, $M_T < 100\,\text{GeV}$, $p_T^{\text{sum}} < 0.2 \times p_T^{\text{lep}}$
Veto track	$p_T > 10\,\text{GeV}$, $|\eta| < 2.4$, $M_T < 100\,\text{GeV}$, $p_T^{\text{sum}} < 0.1 \times p_T^{\text{lep}}$

Collision events are selected using triggers with varied requirements on H_T, p_T^{miss}, H_T^{miss}, and jet p_T. The combined trigger efficiency, measured with a data sample of events with an isolated electron is found to be >98% across the full kinematic range of the search. To suppress the background from SM multi-jet production, we require $M_{T2} > 200$ GeV in events with at least two jets. The minimum M_{T2} threshold is increased to 400 GeV for events with $H_T > 1500$ GeV to maintain SM multi-jet processes as a sub-dominant background in all search regions. To protect against jet mis-measurement, we require that the minimum difference in azimuthal angle between the $\vec{p}_T^{\text{miss}}$ vector and each of the leading four jets, $\Delta\phi_{\text{min}}$, is greater than 0.3 radians, and that the magnitude of the difference between $\vec{p}_T^{\text{miss}}$ and $\vec{H}_T^{\text{miss}}$ is less than half of p_T^{miss}. For the determination of $\Delta\phi_{\text{min}}$ we consider jets with $|\eta| < 4.7$.

Events containing at least two jets are categorized by the values of N_j, N_b, and H_T. Each such bin is referred to as a *topological region*. Signal regions are defined by further dividing topological regions in bins of M_{T2}. Events with only one jet are selected if the p_T of the jet is at least 250 GeV, and are classified according to the transverse momentum of this jet and whether the event contains a b-tagged jet. The search regions are summarized in Tables 5-7 in Appendix A. We also define *super signal regions*, covering a subset of the kinematic space of the full analysis with simpler inclusive selections. These regions can be used to obtain approximate interpretations of our result, as discussed further in Section 5, where the super signal regions are defined.

Monte Carlo (MC) simulations are used to design the search, to aid in the estimation of SM backgrounds, and to evaluate the sensitivity to scenarios of gluino and squark pair production in simplified models of SUSY. Samples of simulated events are produced at either leading order or next-to-leading order using the same generator and simulation packages and the same chain of reconstruction programs as Ref. [5]. The most precise available cross section calculations are used to normalize the SM simulated samples, corresponding most often to next-to-next-to-leading order (NNLO) accuracy.

To improve on the MadGraph [19] modeling of the multiplicity of additional jets from initial state radiation (ISR), Madgraph $t\bar{t}$ Monte Carlo events are reweighted based on the number of ISR jets (N_j^{ISR}) so as to make the jet multiplicity agree with data. The same reweighting procedure is applied to SUSY Monte Carlo events. The reweighting factors vary between 0.92 and 0.51 for N_j^{ISR} between 1 and 6. We take one half of the deviation from unity as the systematic uncertainty on these reweighting factors.

4 Backgrounds

A jets plus p_T^{miss} final state is populated by three categories of SM processes:

- "lost lepton", i.e. events with a lepton from a W decay where the lepton is either out of acceptance, not reconstructed, not identified, or not isolated. This background comes from both W+jets and $t\bar{t}$+jets events.

- "irreducible", i.e. Z+jets events where the Z boson decays to neutrinos. This background is most similar to potential signals. It is a major background in nearly all search regions, its importance decreasing with increasing N_b.

- "instrumental background", i.e. mostly QCD multi-jet events with no real p_T^{miss}. These events enter a search region due to either significant jet momentum over-measurement, under-measurement, or sources of anomalous noise.

4.1 Estimation of the background from leptonic W boson decays

Control regions with exactly one lepton candidate are selected using the same triggers and baseline selections as for the signal regions, with the exception of the lepton veto which is inverted. Selected events are binned according to the same criteria as the search regions, and the background in each signal bin, N_{LL}^{SR}, is obtained from the number of events in the control region, $N_{1\ell}^{CR}$, using transfer factors according to equation 2.

$$N_{LL}^{SR}\left(H_T, N_j, N_b, M_{T2}\right) = N_{1\ell}^{CR}\left(H_T, N_j, N_b, M_{T2}\right) \times R_{MC}^{0\ell/1\ell}\left(H_T, N_j, N_b, M_{T2}\right) \times k\left(M_{T2}\right) \quad (2)$$

The factor $R_{MC}^{0\ell/1\ell}\left(H_T, N_j, N_b, M_{T2}\right)$ accounts for lepton acceptance and efficiency and the expected contribution from the decay of W bosons to hadrons through an intermediate τ lepton.

It is obtained from MC and corrected for measured differences between data and simulation.

The estimated distribution of lost lepton events among M_{T2} bins within a topological region is obtained using both data and simulation as follows. In each topological region, the control region corresponding to the highest M_{T2} bin is successively combined with the previous bin until the expected MC yield in combined bins is at least 50 events. When two or more control region bins are combined, the fraction of events expected to populate a particular M_{T2} bin, $k\,(M_{T2})$, is determined using the expectation from simulated samples. Uncombined bins within each topological region are used to estimate the lost lepton background in the corresponding signal bin (i.e. $k\,(M_{T2}) = 1$ for these bins). For events with $N_j = 1$, a control region is defined for each bin of jet p_T. The modeling of M_{T2} is checked in data using single lepton control samples enriched in events originating from either W+jets or $t\bar{t}$+jets as shown in the left and right panels of Fig. 1, respectively. The predicted distributions in the comparison are obtained by summing all control regions after normalizing MC yields to data and distributing events amongst M_{T2} bins using shapes obtained from simulation, as is done for the estimate of the lost lepton background.

Uncertainties from the limited size of the control sample and from variations of all relevant theoretical and experimental quantities are evaluated and propagated to the final estimate. The dominant uncertainty on the factor $R_{MC}^{0\ell/1\ell}\,(H_T, N_j, N_b, M_{T2})$ arises from the modeling of the lepton efficiency and jet energy scale (JES) and is of order 15–20%. The uncertainty on the M_{T2} extrapolation, as large as 40%, comes primarily from the JES, the relative composition of W+jets and $t\bar{t}$+jets, and variations of the renormalization and factorization scales. These and other uncertainties are similar to those in Ref. [5].
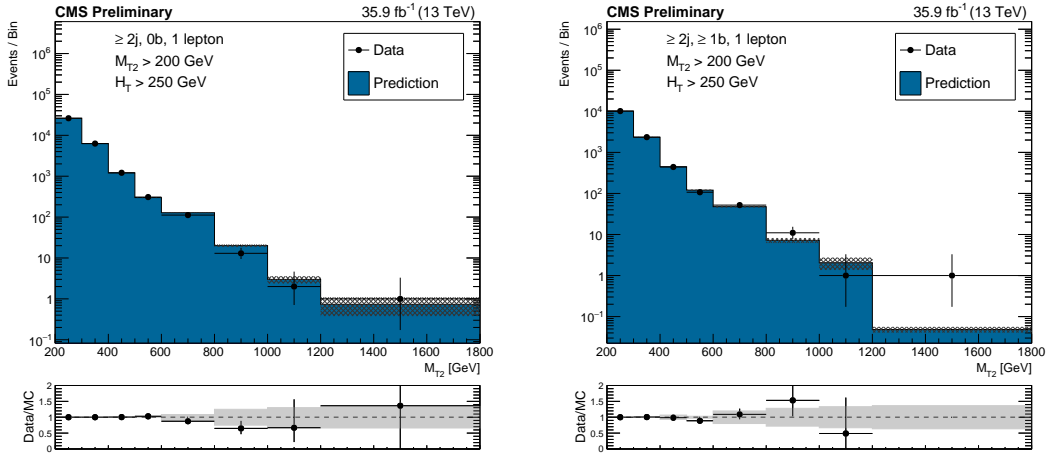

Figure 1: Distributions of data and MC predictions for the single lepton control region selection, after MC is normalized to data in the control region bins of H_T, N_j, and N_b, and M_{T2} shapes are used, for events with no b-tags (left), and events with at least one b-tag (right). The hashed bands on the lost lepton histogram show the MC statistical uncertainty, while the solid gray band on the ratio plot shows the systematic uncertainty on the M_{T2} shape.

4.2   Estimation of the background from $Z(\nu\bar{\nu})$+jets

The $Z \to \nu\bar{\nu}$ background is estimated from a dilepton control sample selected using triggers requiring two leptons. The trigger efficiency, measured with a data sample of events with large H_T, is found to be greater than 97% in the selected kinematic range. To obtain a control sample enriched in $Z \to \ell\ell$ events, we require that the leptons are the same flavor and that the invariant

mass of the lepton pair is consistent with the mass of a Z boson. After requiring that the p_T of the dilepton system is at least 200 GeV, the full baseline selection requirements are applied based on kinematic variables re-calculated after removing the dilepton system from the event to replicate the $Z \to \nu\bar{\nu}$ kinematics. For events with $N_j = 1$, one control region is defined for each bin of jet p_T. For events with at least two jets, the selected events are binned in the H_T, N_j, and N_b dimensions but not in M_{T2} to increase the dilepton event yield in each control region.

The contribution to each control region from flavor-symmetric processes, most importantly $t\bar{t}$, is estimated using opposite flavor (OF) eμ events obtained with the same selections as the same flavor (SF) sample of ee and $\mu\mu$ events. The background in each signal bin is then obtained using transfer factors according to:

$$
\begin{aligned}
N_{Z\to\nu\bar{\nu}}^{SR}\left(H_T, N_j, N_b, M_{T2}\right) = &\left[N_{\ell\ell}^{CRSF}\left(H_T, N_j, N_b\right) - N_{\ell\ell}^{CROF}\left(H_T, N_j, N_b\right) \times R^{SF/OF}\right] \\
&\times R_{MC}^{Z\to\nu\bar{\nu}/Z\to\ell\ell}\left(H_T, N_j, N_b\right) \times k\left(M_{T2}\right)
\end{aligned}
\tag{3}
$$

Here $N_{\ell\ell}^{CRSF}$ and $N_{\ell\ell}^{CROF}$ are the number of SF and OF events in the control region, while $R_{MC}^{Z\to\nu\bar{\nu}/Z\to\ell\ell}$ and $k\left(M_{T2}\right)$ are defined below. The factor $R^{SF/OF}$ accounts for the difference in acceptance and efficiency between the SF and OF samples. It is determined as the ratio of the number of SF events to OF events in a $t\bar{t}$ enriched control sample, obtained with the same selections as the $Z \to \ell\ell$ sample, but inverting the requirements on the p_T and invariant mass of the lepton pair. A measured value of $R^{SF/OF} = 1.13 \pm 0.15$ is observed to be stable with respect to event kinematics and is applied in all regions. Fig. 2 (left) shows $R^{SF/OF}$ measured in bins of the number of jets.
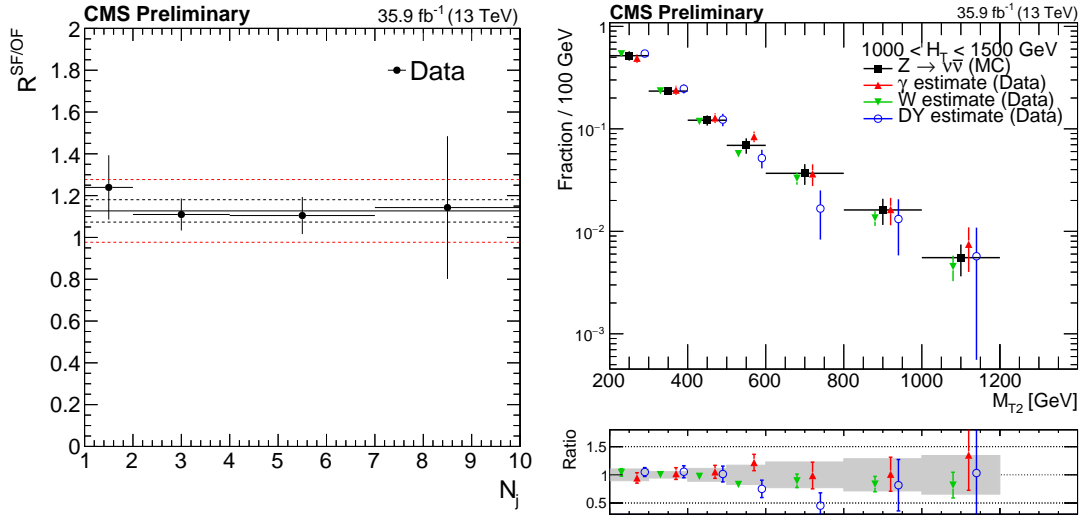

Figure 2: (Left) Ratio $R^{SF/OF}$ in data as a function of N_j. The solid black line enclosed by the red band corresponds to a value of 1.13 ± 0.15 that is observed to be stable with respect to event kinematics, while the two dashed black lines denote the statistical uncertainty on the $R^{SF/OF}$ value. (Right) The shape of the M_{T2} distribution from $Z \to \nu\bar{\nu}$ simulation compared to shapes from γ, W, and Z data control samples in a region with $1000 < H_T < 1500$ GeV and $N_j \geq 2$, and inclusive in N_b. The solid gray band on the ratio plot shows the systematic uncertainty on the M_{T2} shape.

An estimate of the $Z \to \nu\bar{\nu}$ background in each topological region is obtained from the cor-

responding dilepton control region via the factor $R_{\text{MC}}^{Z\to\nu\bar{\nu}/Z\to\ell\ell}$, which accounts for the acceptance and efficiency to select the dilepton pair and the relative branching ratios of $Z \to \ell\ell$ and $Z \to \nu\bar{\nu}$. This factor is obtained from MC after correcting for MC-to-data differences in lepton efficiency.

The normalized M_{T2} distribution, $k\,(M_{\text{T2}})$, is used to obtain the estimate in each search bin. This distribution is constructed using the M_{T2} shape from dilepton data and $Z \to \nu\bar{\nu}$ MC in each topological region. Studies with simulated samples indicate that the M_{T2} shape for $Z \to \nu\bar{\nu}$ events is independent of N_{b} for a given H_{T} selection, and that the shape is also independent of the number of jets for $H_{\text{T}} > 1500\,\text{GeV}$. As a result, the M_{T2} templates for topological regions differing only in N_{b} are combined, separately for data and MC. For $H_{\text{T}} > 1500\,\text{GeV}$, only one M_{T2} template is constructed for data and one for MC by combining all relevant topological regions.

Starting from the highest M_{T2} bin in each control region, we merge bins until the sum of the merged bins contains at least 50 events expected as determined with simulated samples. The fraction of events in each uncombined bin is determined using the corresponding M_{T2} template built from dilepton data events after correcting by the ratio $R_{\text{MC}}^{Z\to\nu\bar{\nu}/Z\to\ell\ell}$. The M_{T2} shape from simulation is used to distribute events among the combined bins, after renormalizing MC to the data yield in the same group of bins.

The modeling of M_{T2} is validated in data using control samples enriched in γ, $W \to \ell\nu$, and $Z \to \ell\ell$ events. The right panel of Fig. 2 shows good agreement between the M_{T2} distribution obtained from γ, W, and Z data control samples with that from $Z \to \nu\bar{\nu}$ MC for events with $1000 < H_{\text{T}} < 1500\,\text{GeV}$. In this comparison, the γ sample is corrected for contributions from multi-jet events and $R_{\text{MC}}^{Z/\gamma}$, the W sample is corrected for top contamination and $R_{\text{MC}}^{Z/W}$, and the Z sample is corrected for top contamination and $R_{\text{MC}}^{Z\to\nu\bar{\nu}/Z\to\ell\ell}$. Here $R_{\text{MC}}^{Z/\gamma}$ ($R_{\text{MC}}^{Z/W}$) is the ratio of the distributions for Z and γ (W) events derived in MC, including the corrections mentioned above.

The largest uncertainty in the estimate of the invisible Z background in most regions results from the limited data statistics of the dilepton control sample. This and all relevant theoretical and experimental quantities are evaluated and propagated to the final estimate. The dominant uncertainty on the ratio $R_{\text{MC}}^{Z\to\nu\bar{\nu}/Z\to\ell\ell}$ comes from measured differences in lepton efficiency between data and simulation and is of order 5%. The uncertainty on the $k\,(M_{\text{T2}})$ factor arises from data statistics for uncombined bins, while for combined bins it is due to uncertainties in the jet energy scale and variations in the renormalization and factorization scales. These can result in effects as large as 40%.

4.3 Estimation of the multi-jet background

For events with at least two jets, a multi-jet enriched control region is obtained in each H_{T} bin by inverting the $\Delta\phi_{\text{min}}$ requirement described in Section 3. Events are selected using H_{T} triggers and the extrapolation from low to high $\Delta\phi_{\text{min}}$ is based on the following ratio:

$$r_{\phi}(M_{\text{T2}}) = N(\Delta\phi_{\text{min}} > 0.3)/N(\Delta\phi_{\text{min}} < 0.3). \tag{4}$$

The ratio can be described by a power law as $r_{\phi}(M_{\text{T2}}) = a \cdot M_{\text{T2}}^{b}$. The parameters a and b are determined separately in each H_{T} bin by fitting r_{ϕ} in an M_{T2} sideband in data after subtracting non-QCD contributions using simulation. The sideband spans M_{T2} values of 60-100 GeV for events with $H_{\text{T}} < 1000$ GeV and 70-100 GeV for events with larger values of H_{T}. The fit to

the r_ϕ distribution in the $1000 < H_T < 1500$ GeV region is shown in Fig. 3 (left). The inclusive multi-jet contribution in each signal region, $N_{j,b}^{SR}(M_{T2})$, is estimated using the ratio $r_\phi(M_{T2})$ measured in the M_{T2} sideband and the number of events in the low $\Delta\phi_{min}$ control region, $N_{inc}^{CR}(M_{T2})$ according to:

$$N_{j,b}^{SR}(M_{T2}) = N_{inc}^{CR}(M_{T2}) \cdot r_\phi(M_{T2}) \cdot f_j(H_T) \cdot r_b(N_j), \qquad (5)$$

where f_j is the fraction of QCD events falling in bin N_j, and r_b is the fraction of events in bin N_j that fall in bin N_b. (Here N_j denotes a jet multiplicity bin, and N_b denotes a b jet multiplicity bin within N_j). The values of f_j and r_b are measured using events with an M_{T2} value between 100 and 200 GeV in the low $\Delta\phi_{min}$ sideband, where f_j is measured separately in each H_T bin while r_b is measured in bins of N_j, integrated over H_T, as r_b is found to be independent of the latter. Values of f_j and r_b measured in data are shown in Fig. 3 (center, right) compared to simulation. Uncertainties from the limited size of the control sample and from variations of the fit and the sample composition are evaluated and found to be of similar size as in Ref. [5], varying between 40 and 180%, depending on the search region.
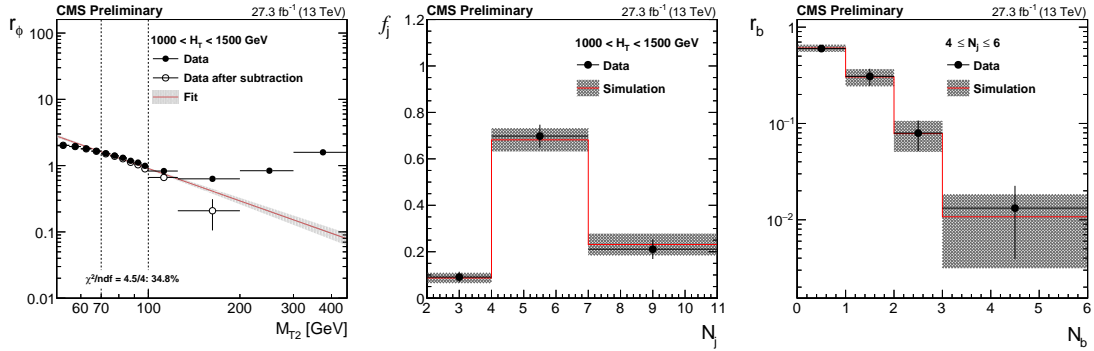

Figure 3: Distribution of the ratio r_ϕ as a function of M_{T2} for the region $1000 < H_T < 1500$ GeV (left). The fit is performed to the hollow, background-subtracted data points. The full points represent the data before subtracting non-QCD backgrounds using simulation. Data point uncertainties are statistical only. The red line and the band around it show the result of the fit to a power-law function perfomed in the window $70 < M_{T2} < 100$ GeV and the associated fit uncertainty. Values of f_j, the fraction of events in bin N_j, (center) and r_b, the fraction of events that fall in bin N_b, (right) are measured in data after requiring $\Delta\phi_{min} < 0.3$ radians and $100 < M_{T2} < 200$ GeV. The bands represent both statistical and systematic uncertainties.

An estimate based on $r_\phi(M_{T2})$ is not viable in the monojet search regions so a different strategy is employed. A control region is obtained by asking for a second jet with $30 < p_T < 60$ GeV and inverting the $\Delta\phi_{min}$ requirement. After subtracting non-QCD contributions using simulation, the data yield in the control region is taken as an estimate of the background in the corresponding monojet search region. Closure tests in simulation show the method provides a conservative estimate of the multi-jet background, which is less than 8% in all monojet search regions. In all monojet bins, a 50% uncertainty in the non-QCD subtraction is combined with the uncertainty in the data yield in the control region with a second jet.

5 Results

The data yields in the search regions are statistically compatible with the estimated backgrounds from SM processes. A summary of the result of this search is shown in Fig. 4. Each bin

in the upper panel corresponds to a single H_T, N_j, N_b topological region integrated over M_{T2}. The lower panel further breaks down the background estimates and observed data yields into M_{T2} bins for the region $575 < H_T < 1000$ GeV. The background estimates and corresponding uncertainties shown in these plots rely exclusively on the inputs from control samples and simulation described in Section 4 and are indicated in the rest of the text as "pre-fit background" results. Distributions for the other H_T regions can be found in Appendix B.

To allow simpler reinterpretation, we also provide results for super signal regions, which cover subsets of the full analysis with simpler inclusive selections and can be used to obtain approximate interpretations of this search. The definitions of these regions are given in Table 2, with the predicted and observed number of events and the 95% confidence level (CL) upper limit on the number of signal events contributing to each region. Limits are set using a modified frequentist approach, employing the CL$_s$ criterion and an asymptotic formulation [20–23]. The 95% CL upper limit on the signal cross section obtained using the most sensitive super signal region is typically less stringent by a factor of $\sim 1.5 - 3$ compared to the full analysis binning.

Table 2: Definitions of super signal regions, along with predictions, observed data, and the observed 95% CL limit on the number of signal events contributing to each region (N_{95}^{obs}). The limits are shown as a range corresponding to an assumed uncertainty on the signal acceptance of 0-15%. A dash in the selections means that no cut is applied.

Region	N_j	N_b	H_T [GeV]	M_{T2} [GeV]	Prediction	Data	N_{95}^{obs}
2j loose	≥ 2	–	> 1000	> 1200	38.9 ± 11.2	42	26.6–27.8
2j tight	≥ 2	–	> 1500	> 1400	2.9 ± 1.3	4	6.5–6.7
4j loose	≥ 4	–	> 1000	> 1000	19.4 ± 5.8	21	15.8–16.4
4j tight	≥ 4	–	> 1500	> 1400	2.1 ± 0.9	2	4.4–4.6
7j loose	≥ 7	–	> 1000	> 600	$23.5^{+5.9}_{-5.6}$	27	18.0–18.7
7j tight	≥ 7	–	> 1500	> 800	$3.1^{+1.7}_{-1.4}$	5	7.6–7.9
2b loose	≥ 2	≥ 2	> 1000	> 600	$12.9^{+2.9}_{-2.6}$	16	12.5–13.0
2b tight	≥ 2	≥ 2	> 1500	> 600	$5.1^{+2.7}_{-2.1}$	4	5.8–6.0
3b loose	≥ 2	≥ 3	> 1000	> 400	8.4 ± 1.8	10	9.3–9.7
3b tight	≥ 2	≥ 3	> 1500	> 400	2.0 ± 0.6	4	6.6–6.9
7j3b loose	≥ 7	≥ 3	> 1000	> 400	5.1 ± 1.5	5	6.4–6.6
7j3b tight	≥ 7	≥ 3	> 1500	> 400	0.9 ± 0.5	1	3.6–3.7

5.1   Interpretation

The result of the search can be interpreted by performing a maximum-likelihood fit to the data in the signal regions. The fit is carried out under either a background-only or a background+signal hypothesis. The modeling of the backgrounds summarized in Section 5 are an input to the fit procedure. The likelihood is constructed as the product of Poisson probability density functions, one for each signal region, and constraint terms that account for uncertainties in the background estimates and, if considered, the signal yield. The result of the background-only fit, denoted as "post-fit background", is given in Appendix B.

The result of the search is used to constrain specific models of new physics such as the simplified models of SUSY shown in Fig. 5. For each scenario of gluino (squark) pair production, the simplified models assume that all supersymmetric particles other than the gluino (squark) and the lightest neutralino are too heavy to be produced directly, and that the gluino (squark) decays promptly. The models assume that each gluino (squark) decays with a 100% branching fraction into the decay products depicted in Fig. 5. For models in Fig. 5 where the decays of the

two squarks differ, a 50% branching fraction for each decay is assumed. Signal cross sections are calculated at NLO+NLL order in α_s [24–28].

Typical values of the uncertainties in the signal yield for one of the models considered are listed in Table 3. The sources of uncertainties considered and the methods used to evaluate their effect on the interpretation are the same as those in Ref. [5]. Uncertainties due to the luminosity, ISR multiplicity, pileup modeling, and b-tagging and lepton efficiencies are treated as correlated across search bins. Remaining uncertainties are taken as uncorrelated.

Figure 6 shows the exclusion limits at 95% confidence level for gluino mediated bottom-squark, top-squark, and light-flavor squark production. Exclusion limits at 95% confidence level for the direct production of bottom, top, and light-flavor squark pairs are shown in Fig. 7. Direct production of top squarks for three alternate decay scenarios are also considered and exclusion limits at 95% confidence level are shown in Fig. 8. Table 4 summarizes the limits of the supersymmetric particles excluded in the simplified model scenarios considered. These results extend the constraints on gluinos and squarks by about 300 GeV and on $\tilde{\chi}_1^0$ by 200 GeV with respect to those in Ref. [5].

Table 3: Typical values of the signal systematic uncertainties as evaluated for the simplified signal model of gluino mediated bottom squark production, $pp \to \tilde{g}\tilde{g}, \tilde{g} \to b\bar{b}\tilde{\chi}_1^0$. Uncertainties evaluated on other signal models are consistent with these ranges of values.

Source	Typical Values
Luminosity	2.6%
Limited size of MC samples	1–100%
Renormalization and factorization scales	5%
ISR multiplicity	0–30%
B-tagging efficiency, heavy flavor	0–40%
B-tagging efficiency, light flavor	0–20%
Lepton efficiency	0–20%
Jet energy scale	5%
Fast simulation p_T^{miss} modeling	0-5%
Fast simulation pileup modeling	4.6%

Table 4: Summary of 95% CL observed exclusion limits for different SUSY simplified model scenarios. The limit on the mass of the produced sparticle is quoted for a massless LSP, while for the lightest neutralino the best limit on its mass is quoted.

Simplified model	Limit on produced sparticle mass [GeV] for $m_{\tilde{\chi}_1^0} = 0$ GeV	Best limit on LSP mass [GeV]
Direct squark production		
Bottom squark	1175	590
Top squark	1070	550
Single light squark	1050	475
8 degenerate light squarks	1550	775
Gluino mediated production		
$\tilde{g} \to b\bar{b}\tilde{\chi}_1^0$	2025	1400
$\tilde{g} \to t\bar{t}\tilde{\chi}_1^0$	1900	1010
$\tilde{g} \to q\bar{q}\tilde{\chi}_1^0$	1860	1100

6 Summary

This paper presents the result of a search for new physics using events with jets and the M_{T2} variable. Results are based on a 35.9 fb^{-1} data sample of proton-proton collisions at $\sqrt{s} =$ 13 TeV collected in 2016 with the CMS detector. No significant deviations from the standard model expectations are observed. The results are interpreted as limits on the production of new, massive colored particles in simplified models of supersymmetry. We probe gluino masses up to 2025 GeV and LSP masses up to 1400 GeV. Additional interpretations in the context of the pair production of light flavor, bottom, and top squarks are performed, probing masses up to 1550, 1175, and 1070 GeV, respectively, and LSP masses up to 775, 590, and 550 GeV in each scenario.
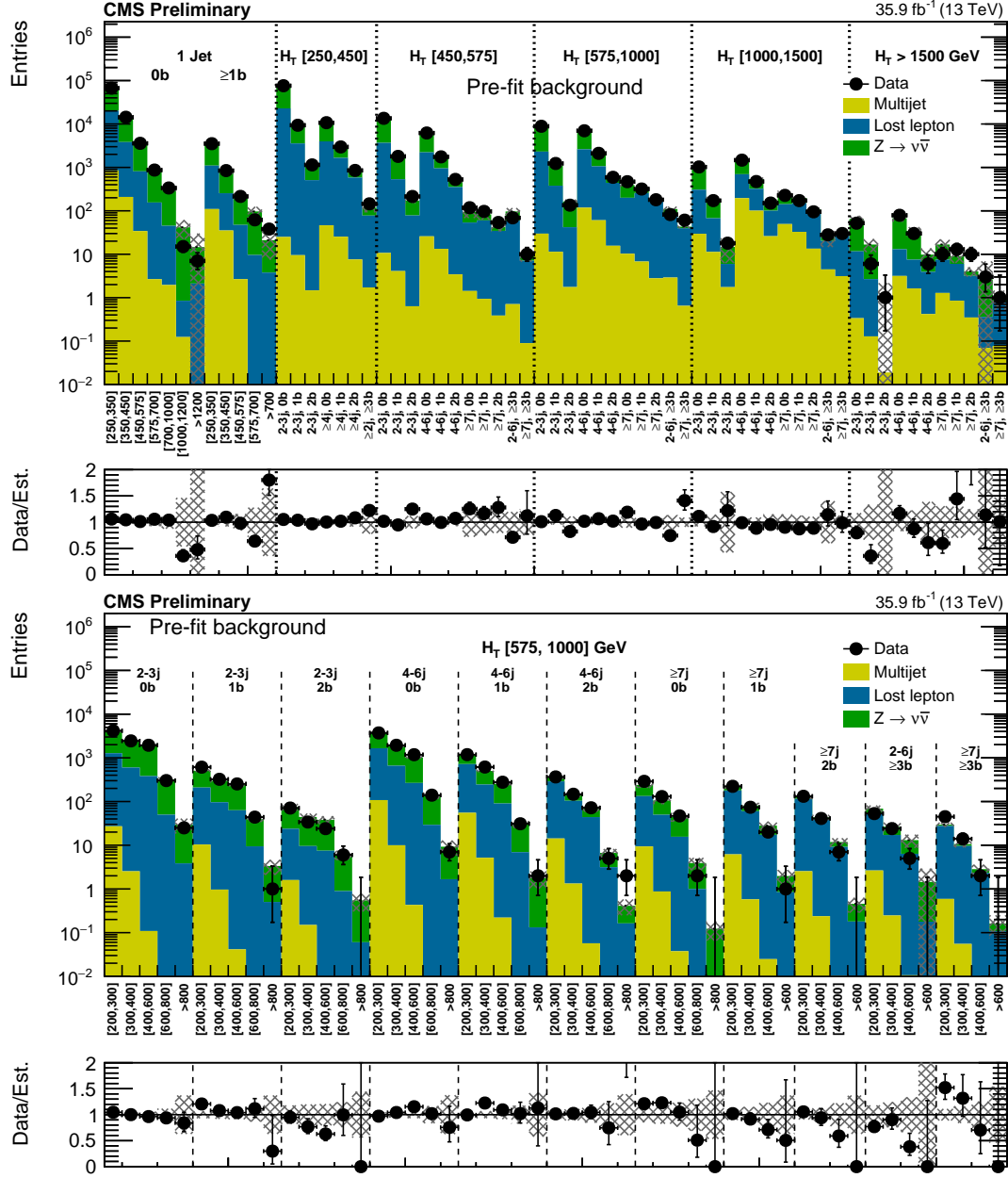
Figure 4: (Above) Comparison of estimated (pre-fit) background and observed data events in each topological region. Hatched bands represent the full uncertainty on the background estimate. The results shown for $N_j = 1$ correspond to the monojet search regions binned in jet p_T, whereas for the multijet signal regions, the notations j, b indicate N_j, N_b labeling. (Below) Same for individual M_{T2} signal bins in the medium H_T region. On the x-axis, the M_{T2} binning is shown (in GeV). Bins with no entry for data have an observed count of 0.
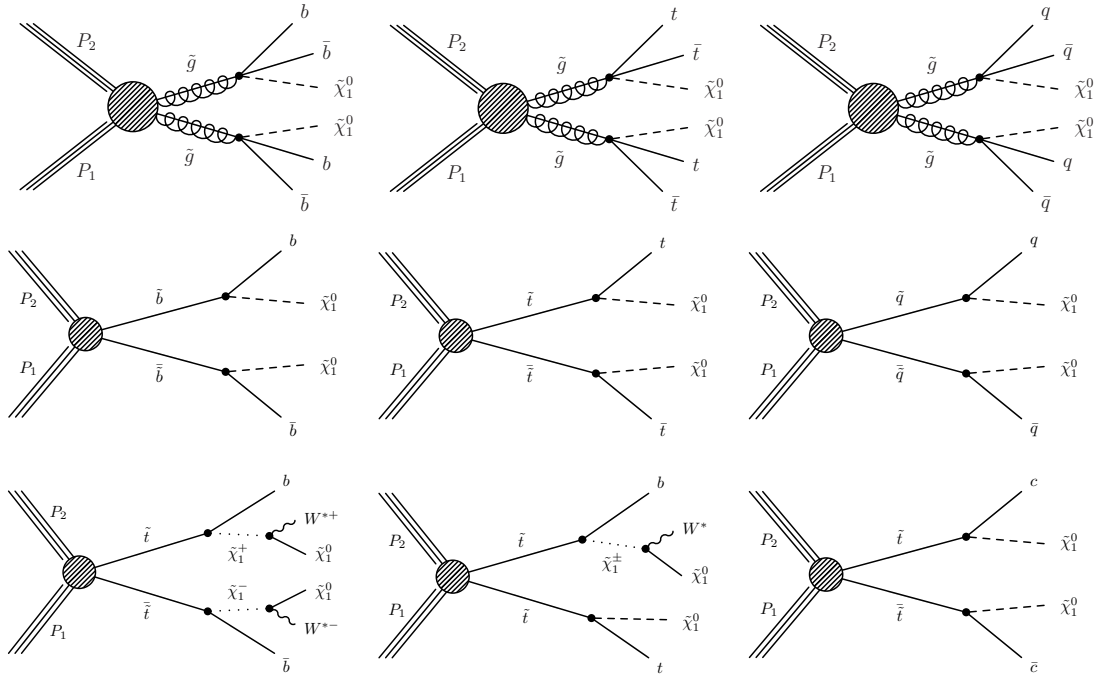
Figure 5: (Top) Diagrams for the three scenarios of gluino mediated bottom squark, top squark and light flavor squark production considered. (Middle) Similar diagrams for the direct production of bottom, top and light flavor squark pairs. (Bottom) Similar diagrams for three alternate scenarios of direct top squark production with different decay modes. For mixed decay scenarios, a 50% branching fraction for each decay is assumed.
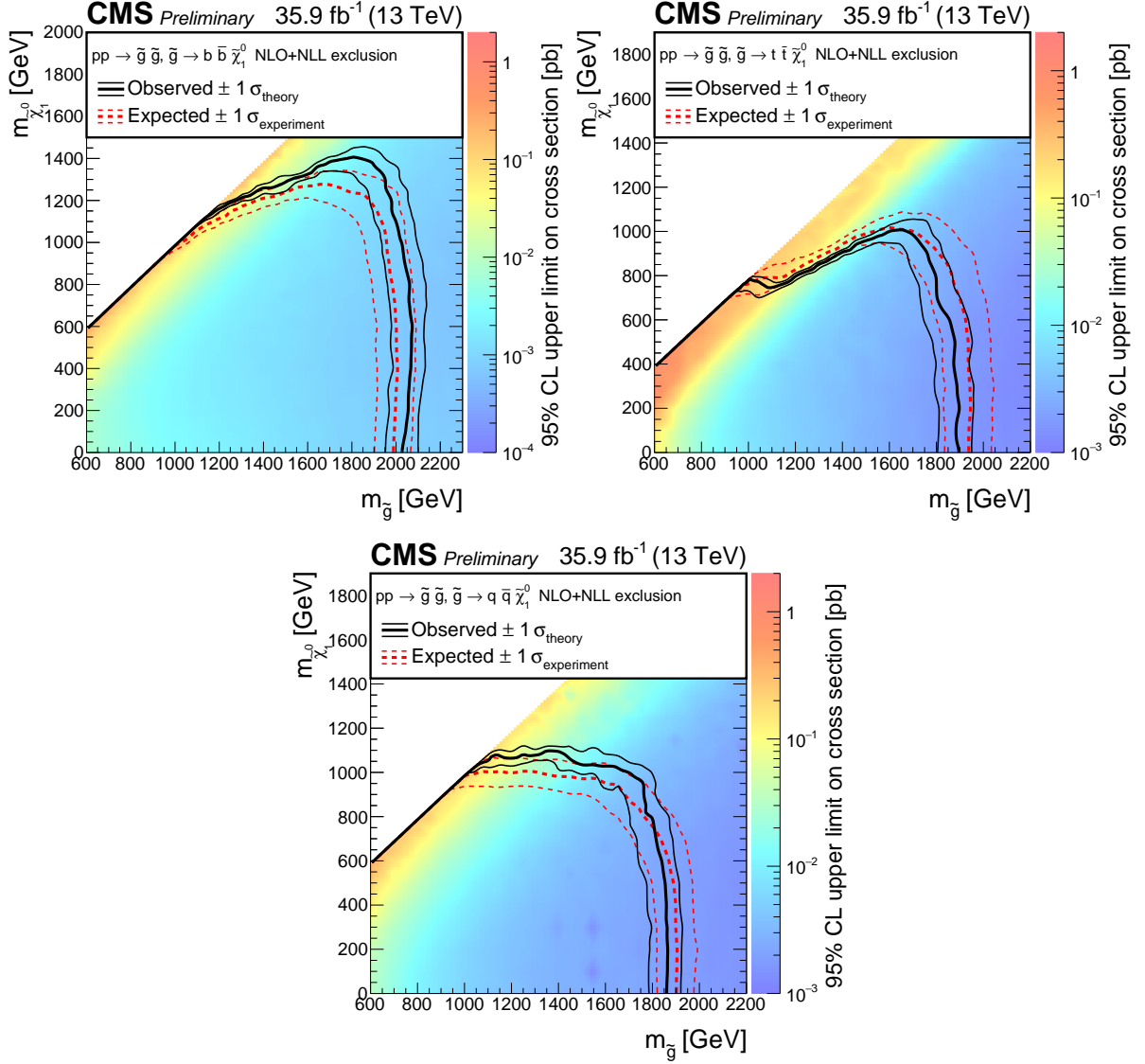
Figure 6: Exclusion limits at 95% CL on the cross sections for gluino-mediated bottom squark production (above left), gluino-mediated top squark production (above right), and gluino-mediated light-flavor squark production (below). The area to the left of and below the thick black curve represents the observed exclusion region, while the dashed red lines indicate the expected limits and their $\pm 1\,\sigma_{\text{experiment}}$ standard deviation uncertainties. The thin black lines show the effect of the theoretical uncertainties σ_{theory} on the signal cross section.
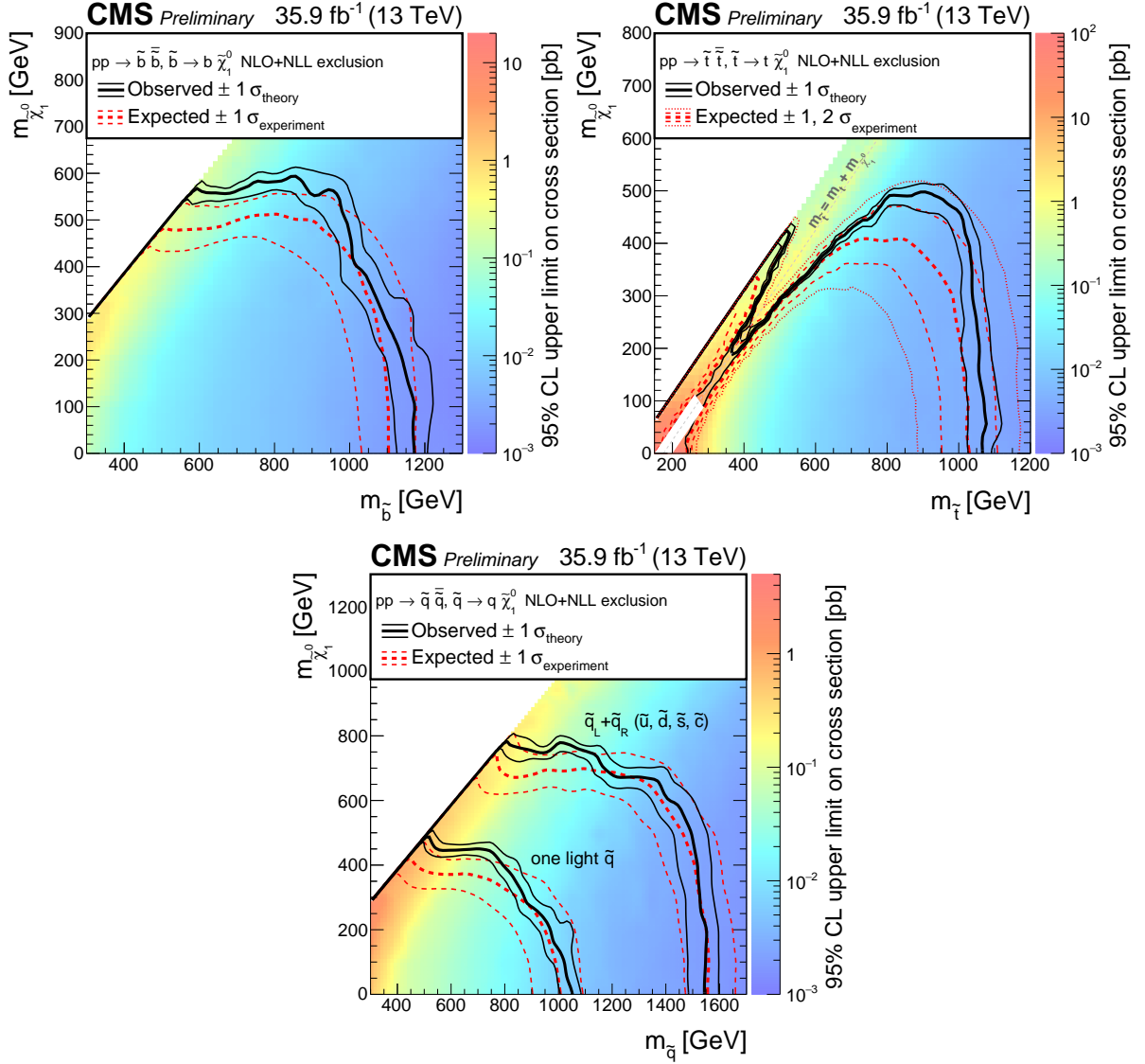
Figure 7: Exclusion limit at 95% CL on the cross sections for bottom squark pair production (above left), top squark pair production (above right), and light-flavor squark pair production (below). The area to the left of and below the thick black curve represents the observed exclusion region, while the dashed red lines indicate the expected limits and their $\pm 1\ \sigma_{\text{experiment}}$ standard deviation uncertainties. For the top squark-pair production plot, the ± 2 standard deviation uncertainties are also shown. The thin black lines show the effect of the theoretical uncertainties σ_{theory} on the signal cross section. The white diagonal band in the upper right plot corresponds to the region $|m_{\tilde{t}} - m_t - m_{\text{LSP}}| < 25\,\text{GeV}$, and small m_{LSP}. Here the efficiency of the selection is a strong function of $m_{\tilde{t}} - m_{\text{LSP}}$, and as a result the precise determination of the cross section upper limit is uncertain because of the finite granularity of the available MC samples in this region of the $(m_{\tilde{t}}, m_{\text{LSP}})$ plane.
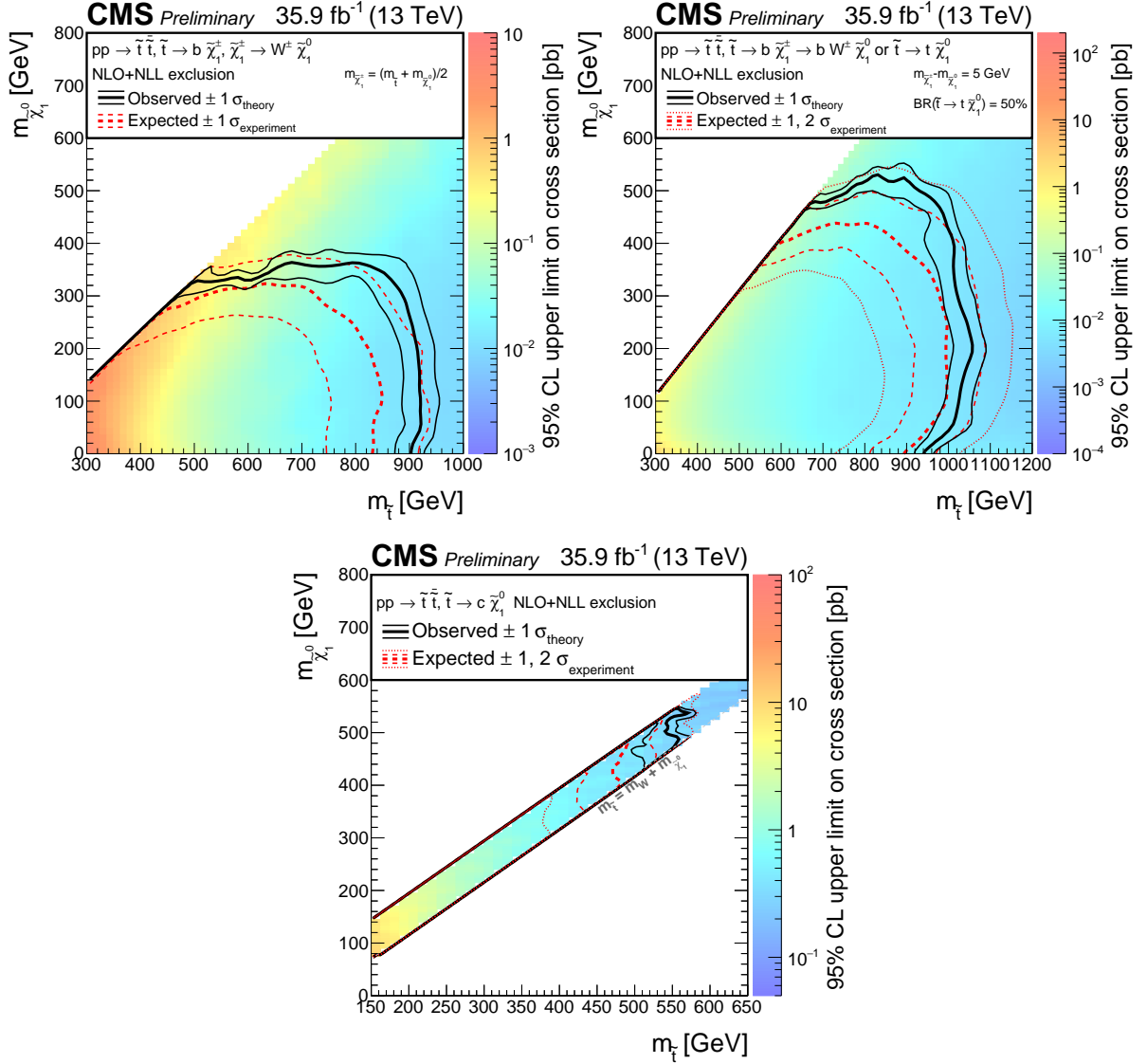
Figure 8: Exclusion limit at 95% CL on the cross sections for top squark pair production for different decay modes of the top squark. For the scenario where $pp \to \tilde{t}_1 \tilde{t}_1^* \to b\bar{b}\tilde{\chi}_1^{\pm}\tilde{\chi}_1^{\mp}$, $\tilde{\chi}_1^{\pm} \to W\tilde{\chi}_1^0$ (above left), the mass of the chargino is chosen to be half way in between the masses of the top squark and the neutralino. A mixed decay scenario (above right), $pp \to \tilde{t}_1 \tilde{t}_1^*$ with equal branching fractions for the top squark decays $\tilde{t}_1 \to t\tilde{\chi}_1^0$ and $\tilde{t}_1 \to b\tilde{\chi}_1^{\pm}$, $\tilde{\chi}_1^{\pm} \to W^*\tilde{\chi}_1^0$, is also considered with the chargino mass chosen such that $\Delta m\left(\tilde{\chi}_1^{\pm}, \tilde{\chi}_1^0\right) = 5\,\text{GeV}$. A compressed scenario (below) is also considered where $pp \to \tilde{t}_1 \tilde{t}_1^* \to c\bar{c}\tilde{\chi}_1^0\tilde{\chi}_1^0$. The area to the left of and below the thick black curve represents the observed exclusion region, while the dashed red lines indicate the expected limits and their $\pm 1\,\sigma_{\text{experiment}}$ standard deviation uncertainties. The thin black lines show the effect of the theoretical uncertainties σ_{theory} on the signal cross section.

References

[1] ATLAS Collaboration, "Search for new phenomena in final states with large jet multiplicities and missing transverse momentum with ATLAS using $\sqrt{s} = 13$ TeV proton-proton collisions", *Phys. Lett.* **B757** (2016) 334–355, `doi:10.1016/j.physletb.2016.04.005`, `arXiv:1602.06194`.

[2] ATLAS Collaboration, "Search for new phenomena in final states with an energetic jet and large missing transverse momentum in pp collisions at $\sqrt{s} = 13$ TeV using the ATLAS detector", `arXiv:1604.07773`.

[3] ATLAS Collaboration, "Search for squarks and gluinos in final states with jets and missing transverse momentum at $\sqrt{s} = 13$ TeV with the ATLAS detector", `arXiv:1605.03814`.

[4] ATLAS Collaboration, "Search for pair production of gluinos decaying via stop and sbottom in events with b-jets and large missing transverse momentum in pp collisions at $\sqrt{s} = 13$ TeV with the ATLAS detector", `arXiv:1605.09318`.

[5] CMS Collaboration, "Search for new physics with the MT2 variable in all-jets final states produced in pp collisions at sqrt(s) = 13 TeV", `arXiv:1603.04053`.

[6] CMS Collaboration, "Search for supersymmetry in the multijet and missing transverse momentum final state in pp collisions at 13 TeV", *Phys. Lett.* **B758** (2016) 152–180, `doi:10.1016/j.physletb.2016.05.002`, `arXiv:1602.06581`.

[7] CMS Collaboration, "Inclusive search for supersymmetry using razor variables in pp collisions at $\sqrt{s} = 13$TeV", *Phys. Rev.* **D95** (2017), no. 1, 012003, `doi:10.1103/PhysRevD.95.012003`, `arXiv:1609.07658`.

[8] CMS Collaboration, "A search for new phenomena in pp collisions at $\sqrt{s} = 13$ TeV in final states with missing transverse momentum and at least one jet using the α_T variable", *Submitted to: Eur. Phys. J. C* (2016) `arXiv:1611.00338`.

[9] C. G. Lester and D. J. Summers, "Measuring masses of semiinvisibly decaying particles pair produced at hadron colliders", *Phys. Lett. B* **463** (1999) 99, `doi:10.1016/S0370-2693(99)00945-4`, `arXiv:hep-ph/9906349`.

[10] CMS Collaboration, "The CMS experiment at the CERN LHC", *JINST* **3** (2008) S08004, `doi:10.1088/1748-0221/3/08/S08004`.

[11] M. Cacciari, G. P. Salam, and G. Soyez, "The anti-k_t jet clustering algorithm", *JHEP* **04** (2008) 063, `doi:10.1088/1126-6708/2008/04/063`, `arXiv:0802.1189`.

[12] M. Cacciari and G. P. Salam, "Pileup subtraction using jet areas", *Phys. Lett. B* **659** (2008) 119, `doi:10.1016/j.physletb.2007.09.077`, `arXiv:0707.1378`.

[13] CMS Collaboration, "Identification of b-quark jets with the CMS experiment", *JINST* **8** (2013) P04013, `doi:10.1088/1748-0221/8/04/P04013`, `arXiv:1211.4462`.

[14] CMS Collaboration, "Missing transverse energy performance of the CMS detector", *JINST* **6** (2011) P09001, `doi:10.1088/1748-0221/6/09/P09001`, `arXiv:1106.5048`.

[15] M. Cacciari, G. P. Salam, and G. Soyez, "The anti-k_t jet clustering algorithm", *JHEP* **04** (2008) 063, doi:10.1088/1126-6708/2008/04/063, arXiv:0802.1189.

[16] M. Cacciari, G. P. Salam, and G. Soyez, "FastJet user manual", *Eur. Phys. J. C* **72** (2012) 1896, doi:10.1140/epjc/s10052-012-1896-2, arXiv:1111.6097.

[17] CMS Collaboration, "Particle-Flow Event Reconstruction in CMS and Performance for Jets, Taus, and MET", CMS Physics Analysis Summary CMS-PAS-PFT-09-001, CERN, 2009.

[18] CMS Collaboration, "Commissioning of the Particle-flow Event Reconstruction with the first LHC collisions recorded in the CMS detector", CMS Physics Analysis Summary CMS-PAS-PFT-10-001, CERN, 2010.

[19] J. Alwall et al., "MadGraph 5: going beyond", *JHEP* **06** (2011) 128, doi:10.1007/JHEP06(2011)128, arXiv:1106.0522.

[20] A. L. Read, "Presentation of search results: The CL_s technique", *J. Phys. G* **28** (2002) 2693, doi:10.1088/0954-3899/28/10/313.

[21] A. L. Read, "Modified frequentist analysis of search results (The CL_s method)", *CERN-OPEN* **205** (2000).

[22] G. Cowan, K. Cranmer, E. Gross, and O. Vitells, "Asymptotic formulae for likelihood-based tests of new physics", *Eur. Phys. J. C* **71** (2011) 1554, doi:10.1140/epjc/s10052-011-1554-0, arXiv:1007.1727.

[23] ATLAS and CMS Collaborations, "Procedure for the LHC Higgs boson search combination in summer 2011", CMS NOTE/ATL-PHYS-PUB ATL-PHYS-PUB-2011-011, CMS-NOTE-2011-005, 2011.

[24] W. Beenakker, R. Höpker, M. Spira, and P. M. Zerwas, "Squark and gluino production at hadron colliders", *Nucl. Phys. B* **492** (1997) 51, doi:10.1016/S0550-3213(97)00084-9, arXiv:hep-ph/9610490.

[25] A. Kulesza and L. Motyka, "Threshold resummation for squark-antisquark and gluino-pair production at the LHC", *Phys. Rev. Lett.* **102** (2009) 111802, doi:10.1103/PhysRevLett.102.111802, arXiv:0807.2405.

[26] A. Kulesza and L. Motyka, "Soft gluon resummation for the production of gluino-gluino and squark-antisquark pairs at the LHC", *Phys. Rev. D* **80** (2009) 095004, doi:10.1103/PhysRevD.80.095004, arXiv:0905.4749.

[27] W. Beenakker et al., "Soft-gluon resummation for squark and gluino hadroproduction", *JHEP* **12** (2009) 041, doi:10.1088/1126-6708/2009/12/041, arXiv:0909.4418.

[28] W. Beenakker et al., "Squark and gluino hadroproduction", *Int. J. Mod. Phys. A* **26** (2011) 2637, doi:10.1142/S0217751X11053560, arXiv:1105.1110.

A   Definition of search regions

The 213 exclusive search regions are defined in Tables 5–7.

Table 5:   Summary of signal regions for the monojet selection.

N_b	jet p_T binning [GeV]
0	[250,350,450,575,700,1000,1200,∞]
≥ 1	[250,350,450,575,700,∞]

Table 6:   Adopted M_{T2} binning in each topological region of the multi-jet search regions, for the very low, low and medium H_T regions.

H_T Range [GeV]	Jet Multiplicities	M_{T2} Binning [GeV]
[250, 450]	$2 - 3j$, 0b	[200, 300, 400, ∞]
	$2 - 3j$, 1b	[200, 300, 400, ∞]
	$2 - 3j$, 2b	[200, 300, 400, ∞]
	$\geq 4j$, 0b	[200, 300, 400, ∞]
	$\geq 4j$, 1b	[200, 300, 400, ∞]
	$\geq 4j$, 2b	[200, 300, 400, ∞]
	$\geq 2j$, $\geq 3b$	[200, 300, 400, ∞]
[450, 575]	$2 - 3j$, 0b	[200, 300, 400, 500, ∞]
	$2 - 3j$, 1b	[200, 300, 400, 500, ∞]
	$2 - 3j$, 2b	[200, 300, 400, 500, ∞]
	$4 - 6j$, 0b	[200, 300, 400, 500, ∞]
	$4 - 6j$, 1b	[200, 300, 400, 500, ∞]
	$4 - 6j$, 2b	[200, 300, 400, 500, ∞]
	$\geq 7j$, 0b	[200, 300, 400, ∞]
	$\geq 7j$, 1b	[200, 300, 400, ∞]
	$\geq 7j$, 2b	[200, 300, 400, ∞]
	$2 - 6j$, $\geq 3b$	[200, 300, 400, 500, ∞]
	$\geq 7j$, $\geq 3b$	[200, 300, 400, ∞]
[575, 1000]	$2 - 3j$, 0b	[200, 300, 400, 600, 800, ∞]
	$2 - 3j$, 1b	[200, 300, 400, 600, 800, ∞]
	$2 - 3j$, 2b	[200, 300, 400, 600, 800, ∞]
	$4 - 6j$, 0b	[200, 300, 400, 600, 800, ∞]
	$4 - 6j$, 1b	[200, 300, 400, 600, 800, ∞]
	$4 - 6j$, 2b	[200, 300, 400, 600, 800, ∞]
	$\geq 7j$, 0b	[200, 300, 400, 600, 800, ∞]
	$\geq 7j$, 1b	[200, 300, 400, 600, ∞]
	$\geq 7j$, 2b	[200, 300, 400, 600, ∞]
	$2 - 6j$, $\geq 3b$	[200, 300, 400, 600, ∞]
	$\geq 7j$, $\geq 3b$	[200, 300, 400, 600, ∞]

Table 7: Adopted M_{T2} binning in each topological region of the multi-jet search regions, for the high and extreme H_{T} regions.

| H_{T} Range [GeV]	Jet Multiplicities	M_{T2} Binning [GeV]
[1000, 1500]	$2 - 3\text{j}, 0\text{b}$	[200, 400, 600, 800, 1000, 1200, ∞]
	$2 - 3\text{j}, 1\text{b}$	[200, 400, 600, 800, 1000, 1200, ∞]
	$2 - 3\text{j}, 2\text{b}$	[200, 400, 600, 800, 1000, ∞]
	$4 - 6\text{j}, 0\text{b}$	[200, 400, 600, 800, 1000, 1200, ∞]
	$4 - 6\text{j}, 1\text{b}$	[200, 400, 600, 800, 1000, 1200, ∞]
	$4 - 6\text{j}, 2\text{b}$	[200, 400, 600, 800, 1000, ∞]
	$\geq 7\text{j}, 0\text{b}$	[200, 400, 600, 800, 1000, ∞]
	$\geq 7\text{j}, 1\text{b}$	[200, 400, 600, 800, ∞]
	$\geq 7\text{j}, 2\text{b}$	[200, 400, 600, 800, ∞]
	$2 - 6\text{j}, \geq 3\text{b}$	[200, 400, 600, ∞]
	$\geq 7\text{j}, \geq 3\text{b}$	[200, 400, 600, ∞]
[1500, ∞]	$2 - 3\text{j}, 0\text{b}$	[400, 600, 800, 1000, 1400, ∞]
	$2 - 3\text{j}, 1\text{b}$	[400, 600, 800, 1000, ∞]
	$2 - 3\text{j}, 2\text{b}$	[400, ∞]
	$4 - 6\text{j}, 0\text{b}$	[400, 600, 800, 1000, 1400, ∞]
	$4 - 6\text{j}, 1\text{b}$	[400, 600, 800, 1000, 1400, ∞]
	$4 - 6\text{j}, 2\text{b}$	[400, 600, 800, ∞]
	$\geq 7\text{j}, 0\text{b}$	[400, 600, 800, 1000, ∞]
	$\geq 7\text{j}, 1\text{b}$	[400, 600, 800, ∞]
	$\geq 7\text{j}, 2\text{b}$	[400, 600, 800, ∞]
	$2 - 6\text{j}, \geq 3\text{b}$	[400, 600, ∞]
	$\geq 7\text{j}, \geq 3\text{b}$	[400, ∞]

B Detailed Results
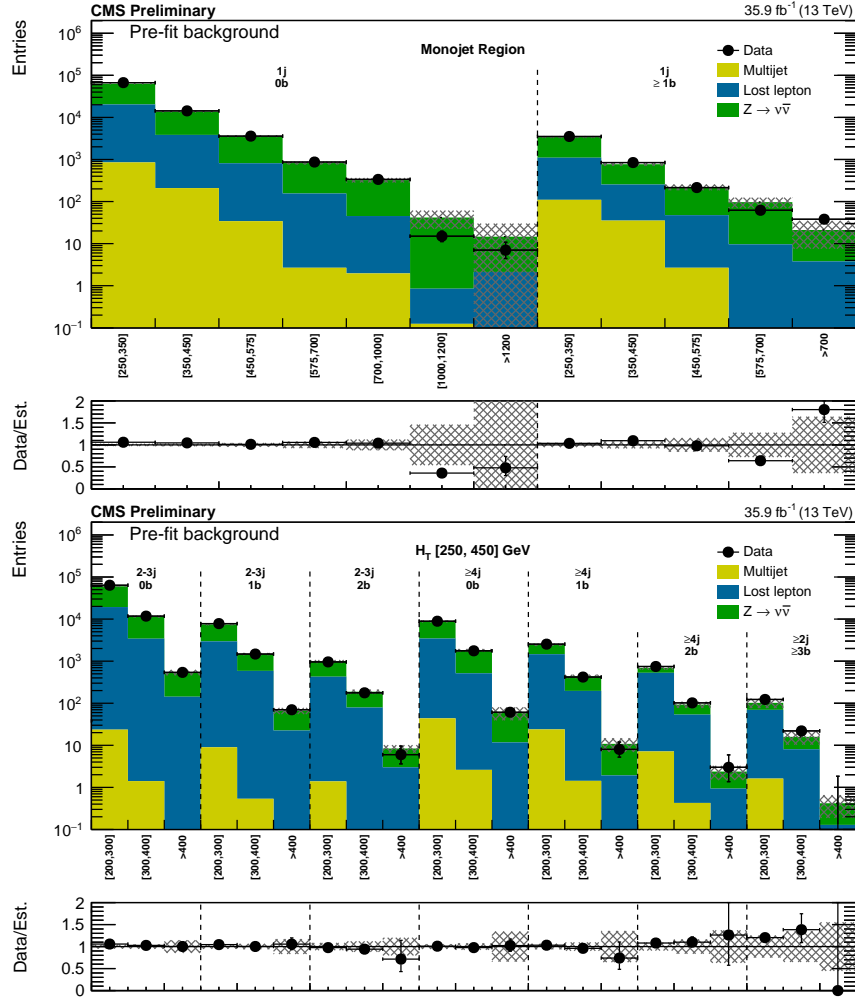
Figure 9: (Above) Comparison of the estimated background and observed data events in each signal bin in the monojet region. On the *x*-axis, the $p_{\mathrm{T}}^{\mathrm{jet1}}$ binning is shown (in GeV). Hatched bands represent the full uncertainty on the background estimate. (Below) Same for the very low H_{T} region. On the *x*-axis, the M_{T2} binning is shown (in GeV). Bins with no entry for data have an observed count of 0.
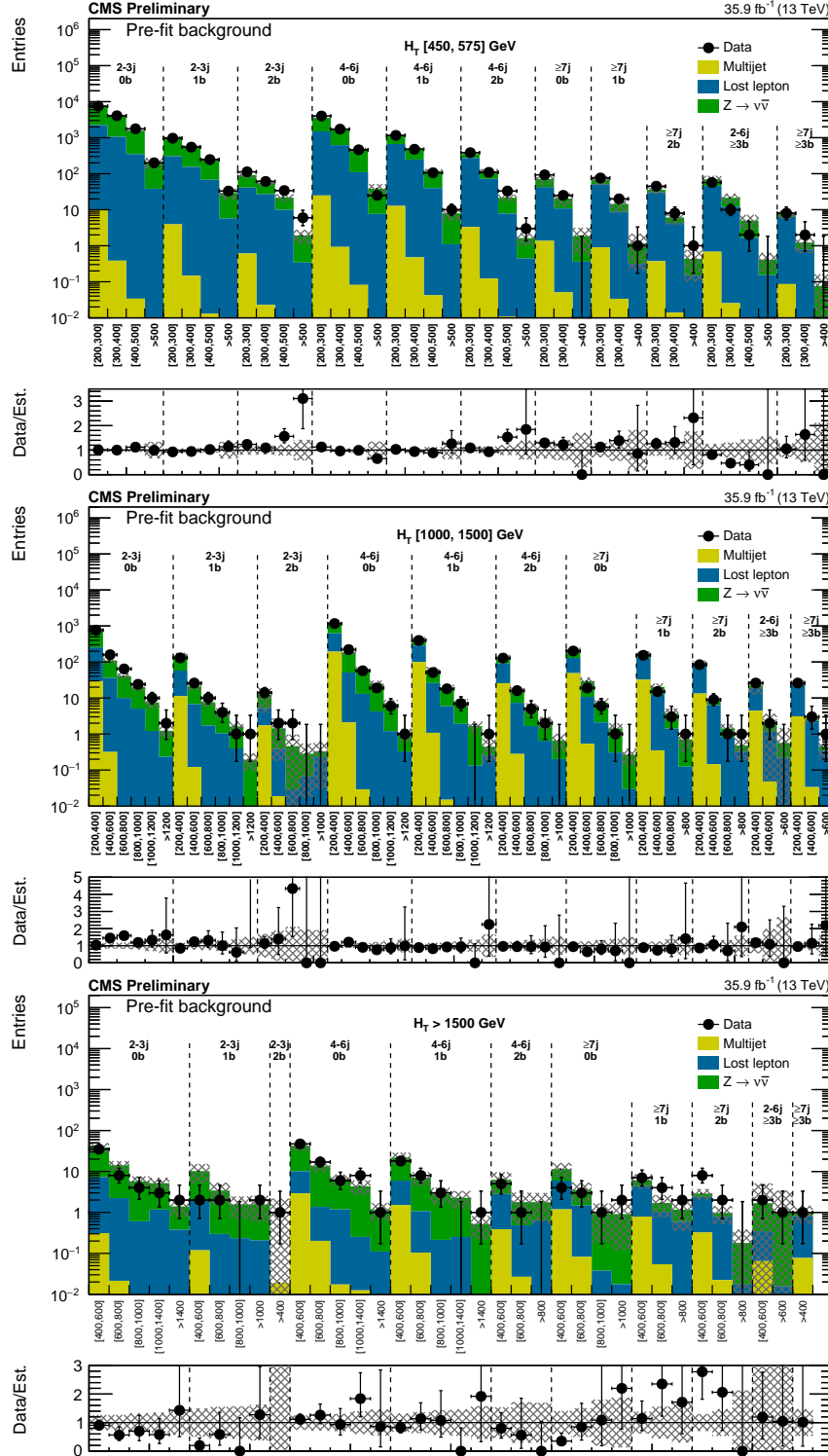
Figure 10: (Top) Comparison of the estimated background and observed data events in each signal bin in the low H_T region. Hatched bands represent the full uncertainty on the background estimate. Same for the high (middle) and extreme (bottom) H_T regions. On the *x*-axis, the M_{T2} binning is shown (in GeV). Bins with no entry for data have an observed count of 0. For the extreme H_T region, the last bin is left empty for visualization purposes.
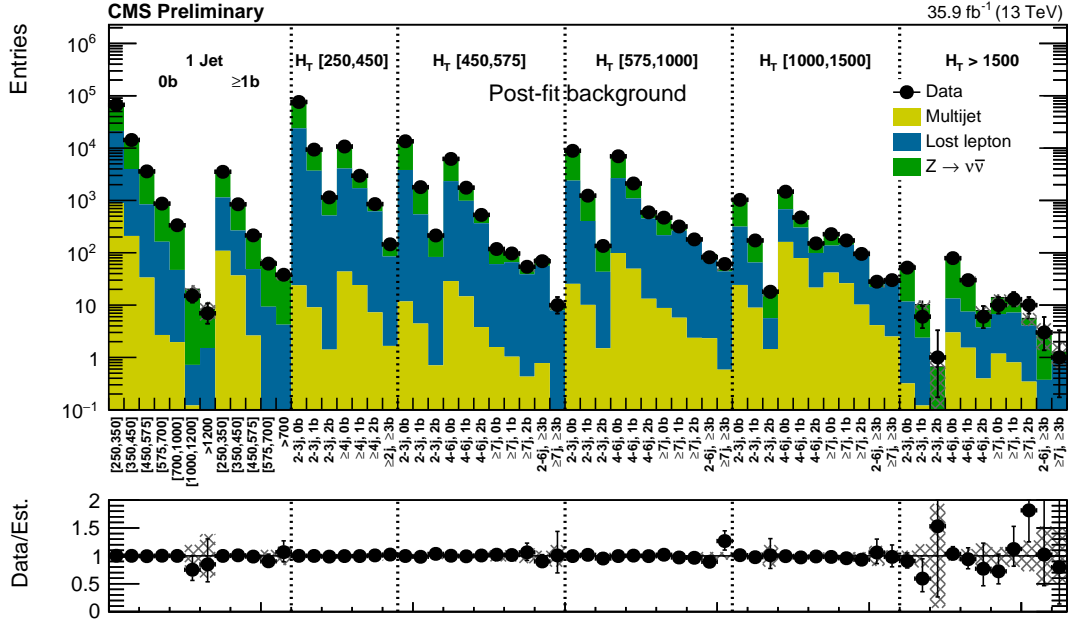
Figure 11: Comparison of post-fit background prediction and observed data events in each topological region. Hatched bands represent the post-fit uncertainty on the background prediction. For the monojet, on the x-axis the p_T^{jet1} binning is shown (in GeV), whereas for the multijet signal regions, the notations j, b indicate N_j, N_b labeling.

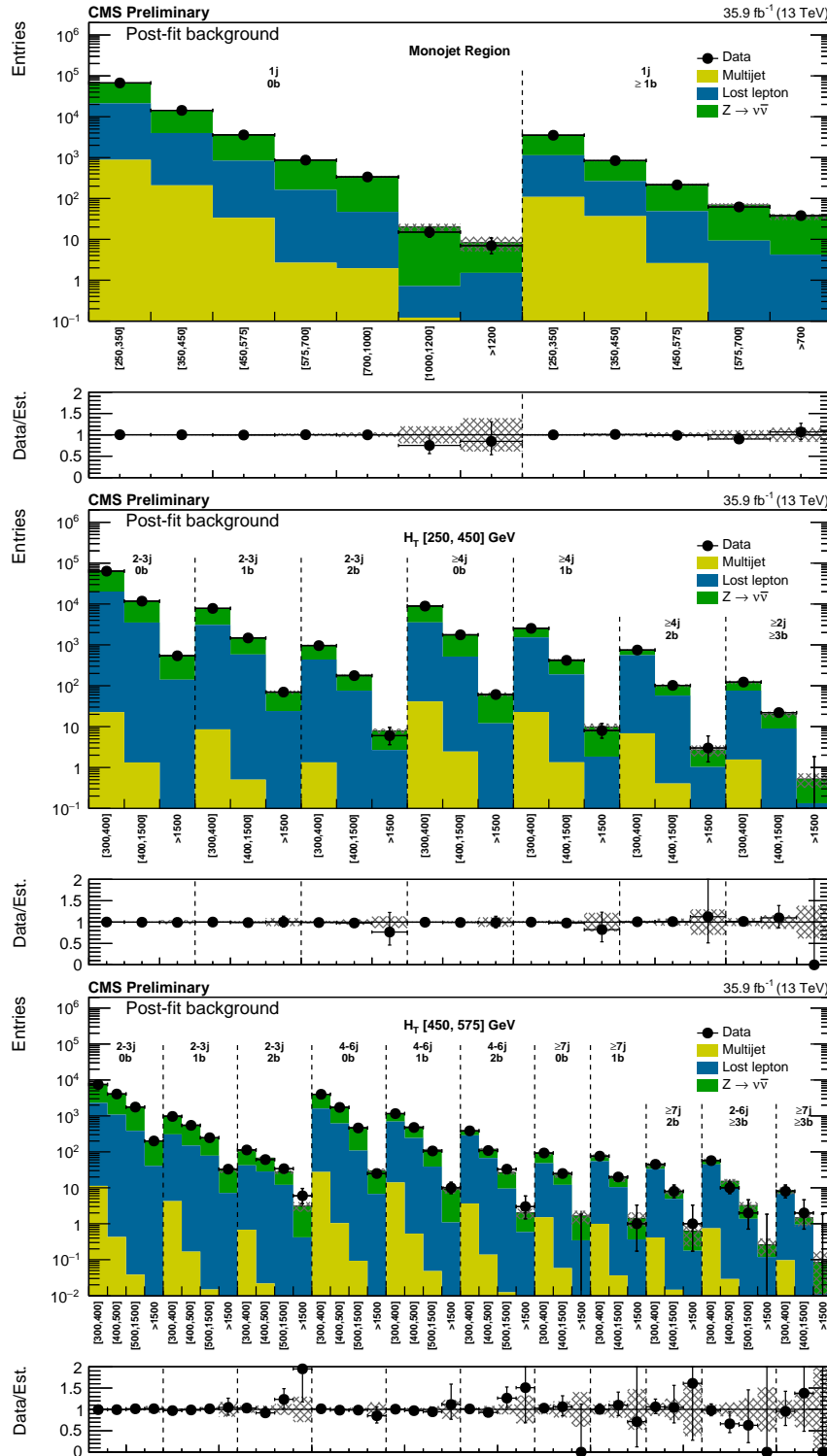Figure 12: (Top) Comparison of the post-fit background prediction and observed data events in each signal bin in the monojet region. On the *x*-axis, the p_T^{jet1} binning is shown (in GeV). (Medium) and (bottom): Same for the very low and low H_T region. On the *x*-axis, the M_{T2} binning is shown (in GeV). Bins with no entry for data have an observed count of 0. In these Figures, the hatched bands represent the post-fit uncertainty on the background prediction.
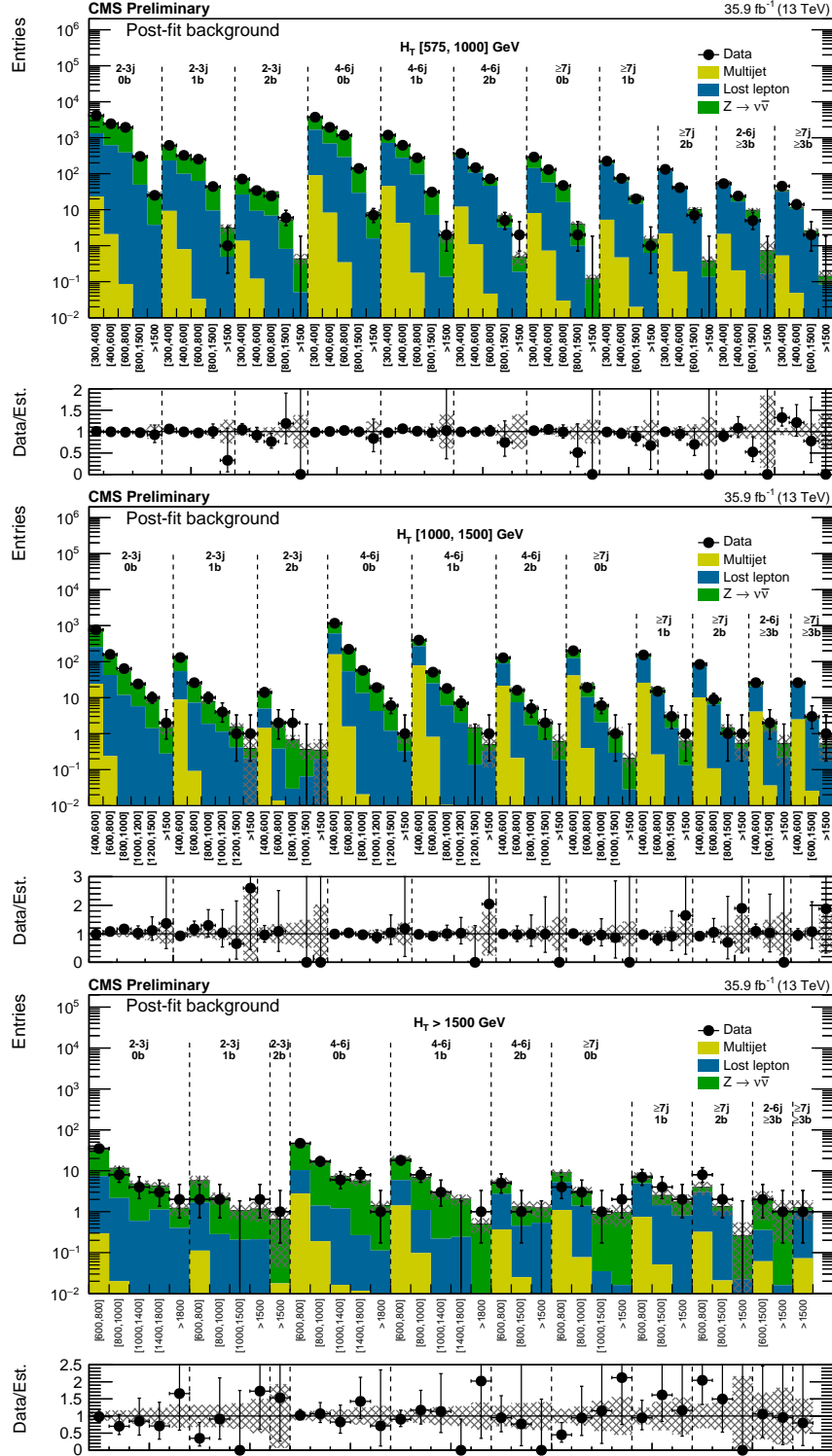
Figure 13: (Top) Comparison of the post-fit background prediction and observed data events in each signal bin in the medium H_T region. Same for the high (middle) and extreme (bottom) H_T regions. On the x-axis, the M_{T2} binning is shown (in GeV). Bins with no entry for data have an observed count of 0. In these Figures, the hatched bands represent the post-fit uncertainty on the background prediction. For the extreme H_T region, the last bin is left empty for visualization purposes.
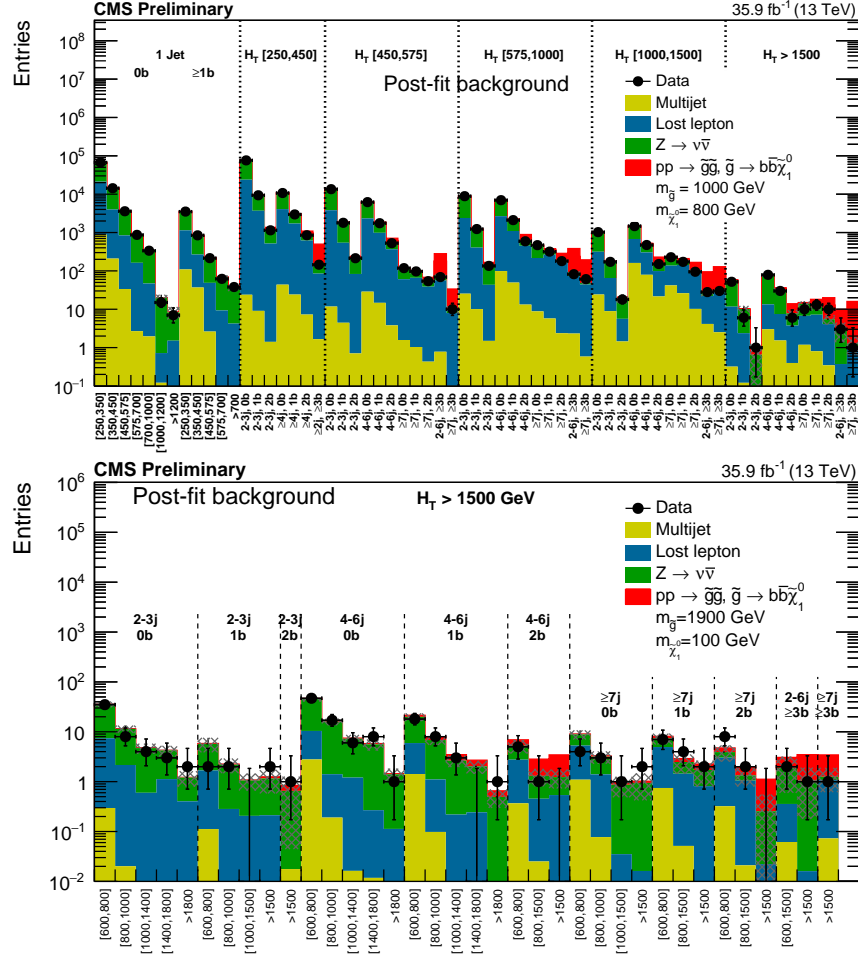
Figure 14: (Above) The post-fit background prediction and observed data events in the analysis binning, for all topological regions with the expected yield for the signal model of gluino mediated bottom-squark production ($m_{\widetilde{g}} = 1000\,\text{GeV}$, $m_{\widetilde{\chi}_1^0} = 800\,\text{GeV}$) stacked on top of the expected background. For the monojet regions, on the x-axis is shown the p_T^{jet1} binning (in GeV). (Below) Same for the extreme H_T region for the same signal with ($m_{\widetilde{g}} = 1900\,\text{GeV}$, $m_{\widetilde{\chi}_1^0} = 100\,\text{GeV}$). In these Figures, the hatched bands represent the post-fit uncertainty on the background prediction. For the extreme H_T region, the last bin is left empty for visualization purposes.